Soft Matter

Accepted Manuscript

This is an *Accepted Manuscript*, which has been through the Royal Society of Chemistry peer review process and has been accepted for publication.

Accepted Manuscripts are published online shortly after acceptance, before technical editing, formatting and proof reading. Using this free service, authors can make their results available to the community, in citable form, before we publish the edited article. We will replace this *Accepted Manuscript* with the edited and formatted *Advance Article* as soon as it is available.

You can find more information about *Accepted Manuscripts* in the Information for Authors.

Please note that technical editing may introduce minor changes to the text and/or graphics, which may alter content. The journal's standard Terms & Conditions and the Ethical guidelines still apply. In no event shall the Royal Society of Chemistry be held responsible for any errors or omissions in this *Accepted Manuscript* or any consequences arising from the use of any information it contains.

ROYAL SOCIETY OF CHEMISTRY

www.rsc.org/softmatter

Journal Name

ARTICLE TYPE

Cite this: DOI: 10.1039/xxxxxxxxxx

Reconstructing the fractal dimension of granular aggregates from light intensity spectra

Fiona H.M. Tang,*[a] and Federico Maggi[a]

Received Date
Accepted Date

DOI: 10.1039/xxxxxxxxxx

www.rsc.org/journalname

There has been a growing interest in using the fractal dimension to study the hierarchical structures of soft materials after realising fractality is an important property of natural and engineered materials. This work presents a method to quantify the internal architecture and the space-filling capacity of granular fractal aggregates by reconstructing the three-dimensional capacity dimension from their two-dimensional optical projections. Use is made of the light intensity of the two-dimensional aggregate images to describe the aggregate surface asperities (quantified by the perimeter-based fractal dimension) and the internal architecture (quantified by the capacity dimension) within a mathematical framework. This method was tested on control aggregates of diffusion-limited (DLA), cluster-cluster (CCA) and self-correlated (SCA) types, stereolithographically-fabricated aggregates, and experimentally-acquired natural sedimentary aggregates. Statistics of reconstructed capacity dimension featured correlation coefficients R $\geq 98\%$, residuals NRMSE $\leq 10\%$ and percent error PE $\leq 4\%$ as compared to controls, and improved earlier approaches by up to 50%.

1 Introduction

The majority of natural and engineered aggregated materials are hierarchically structured over multiple length scales[1], with these hierarchy typically exhibiting statistical self-similarity (e.g., peptide molecules[2–4], proteins[5], crystal and gel networks[6,7], biomaterials[8], nanoparticle clusters[9] and granular materials[10]). Concepts of fractality in analysing hierarchically-structured materials has, therefore, gained great attention in the past decade[3,9] to improve the understanding of macroscopic material property and potentially contribute to the design and synthesis of new materials[1], such as, nanostructures[3]. A fractal architecture can be characterized in many aspects by means of the generalized fractal dimensionality d_q[11–13], which includes the capacity ($q = 0$), correlation ($q = 1$) and information ($q = 2$) dimensions as well as an infinite number of other fractal dimensions (for other moments q). Among these, the capacity dimension d_0 is one of the most important, especially in material science, because it describes the space-filling capability and relates closely to the mass, density and porosity[14,15].

Although direct calculation of the three-dimensional (3D) capacity dimension may be possible with techniques such as electron microscope tomography[16,17], X-ray computed tomography[18], and magnetic resonance interferometry[19,20], these techniques are either capital intensive or hamper measurements when they require the transferring of samples, operation that can affect the sample structures especially during the handling of fragile materials. Hence, there is a need to develop a method that relates the 3D capacity dimension of a body to its two-dimensional (2D) fractal properties assessed from planar images (projections), which can be obtained without physical perturbation of samples and at relatively low cost using CCD and CMOS sensors. While acknowledging the potentially wide range of applications, we give emphasis to granular fractal aggregates in this contribution.

The capacity dimension $d_0(S_2)$ of a 2D image S_2 from a 3D aggregate S_3 with capacity dimension $d_0(S_3)$ is widely accepted to follow the expression[21]

$$d_0(S_2) = \min\{2, d_0(S_3)\}. \quad (1)$$

Inverting Eq. (1) allows to calculate $d_0(S_3) = d_0(S_2)$ when $d_0(S_2) < 2$, while $d_0(S_3)$ is undetermined otherwise. Note that Eq. (1) is an approximation;[22] have given evidence that a projection only preserves information of the dimensionality d_q for the moments $1 < q \leq 2$, thus excluding the capacity dimension d_0 at $q = 0$. In addition, Eq. (1) is valid for indefinitely extended fractal sets, while it fails to describe the relation between $d_0(S_2)$ and $d_0(S_3)$

* Corresponding author
[a] Laboratory for Environmental Engineering, School of Civil Engineering, The University of Sydney, Bld. J05, 2006 Sydney, NSW, Australia. E-mail: fiona.tang@sydney.edu.au, federico.maggi@sydney.edu.au

for compact sets[23–25] such as polymers, granular aggregates and biological cells. As an alternative to Eq. (1),[23] proposed a mathematical expression that estimates $d_0(S_3)$ from the perimeter-based fractal dimension $d_P(S_2)$, which measures the segmentation of the external boundary of S_2. The advantage of using $d_P(S_2)$ is that it is not included in d_q and, therefore, is not subject to any of the above limitations. Application of this equation to numerically-generated diffusion-limited (DLA) and cluster-cluster (CCA) aggregates[25], interstellar medium[24], paramagnetic particles[26] and lime softening flocs[27] showed a significant improvement in retrieving $d_0(S_3)$ as compared to Eq. (1), but it was found to lead to 3 to 10% underestimation of the actual $d_0(S_3)$ for small aggregates with high fractal dimension[25,27]. It is contended here that this underestimation stemmed from the use of the outermost projection segmentation, *i.e.*, $d_P(S_2)$ of the boundary of S_2; to improve the method, we hypothesise here that additional information can be retrieved from the interior part of the projection, when information is readily available such as with modern imaging techniques as explained below.

Light intensity of 2D optical images of soft matter (*e.g.,* granular aggregates) is generally heterogeneous because scattering depends on surface topography, which may itself be a proxy to the internal fractal architecture. Exploiting this information may therefore improve estimation of the capacity dimension $d_0(S_3)$ of 3D aggregates from S_2. We thus contend that the perimeter-based fractal dimension of each intensity contour line, instead of just the outermost boundary of S_2, can be employed to this purpose.

The aim of this work is to put forth a method that uses the light intensity and multiple perimeter segmentations of 2D images to estimate the 3D capacity dimension of aggregates. To achieve this, we first show that projections (images) of aggregates have a characteristic intensity-based $d_P(S_2)$ spectrum; next, we hypothesise that there exists an optimal value of $d_P(S_2)$ that can accurately return $d_0(S_3)$ of that aggregate. Based on this hypothesis, we propose mathematical functions to describe $d_P(S_2)$ spectrum and determine the optimal $d_P(S_2)$, which ultimately provides $d_0(S_3)$ of an aggregate. This method was then tested on aggregates of various origin, including aggregates of diffusion-limited, cluster-cluster, self-correlated, stereolithographically-fabricated aggregates and experimentally-acquired natural sedimentary aggregates.

2 Methods

This section outlines the basis upon which the method was developed and introduces the procedure used to validate it against a control set of numerically-generated and stereolithographically-fabricated aggregates with known $d_0(S_3)$, and experimentally-acquired sedimentary aggregates with benchmark values of $d_0(S_3)$.

2.1 Earlier approach

The method proposed in[23] yields $d_0(S_3)$ of an aggregate from $d_P(S_2)$ of its projection S_2 as

$$d_0(S_3) = \sqrt{\frac{a(\ell)}{d_P(S_2) - b(\ell)}} \text{ for } d_P(S_2) < 2, \tag{2}$$

where $\ell = L/L_p$ is the dimensionless aggregate size with L as the aggregate size and L_p as the primary particle size, and $a(\ell)$ and $b(\ell)$ are the functions

$$a(\ell) = 9\left(z(\ell) - \frac{2[k(\ell)]^2 - 9z(\ell)}{[k(\ell)]^2 - 9}\right), \tag{3a}$$

$$b(\ell) = \frac{2[k(\ell)]^2 - 9z(\ell)}{[k(\ell)]^2 - 9}, \tag{3b}$$

with $z(\ell) = (\log[4\ell - 4])/(\log[\ell])$ and $k(\ell) = z(\ell)[z(\ell) - 1] + 1$. In Eq. (2), $d_P(S_2)$ is defined as[28],

$$d_P(S_2) = 2\frac{\log[N_P]}{\log[N_A]}, \tag{4}$$

where N_P and N_A are the dimensionless perimeter (*i.e.,* the number of pixels at the outermost boundary of S_2) and area of the projection S_2 (*i.e.,* the number of pixels contained within that boundary after filling holes), respectively. Note that $d_P(S_2)$ ranges between $[Z(\ell), 2]$, where $Z(\ell)$ is a function of ℓ defined as[23],

$$Z(\ell) = \begin{cases} 2\frac{\log[\ell]}{\log[\ell]} = 2 & \text{for } \ell = 1, \\ 2\frac{\log[4\ell-4]}{\log[\ell^2]} \leq 2 & \text{for } \ell \geq 2, \\ 1 & \text{for } \ell = \infty. \end{cases} \tag{5}$$

The method proposed in this work improves and extends the approach described above after introducing the following additional quantities.

2.2 Perimeter-based fractal dimension spectrum

Consider the normalized intensity $I \in [0, 1]$ of a grayscale image (projection) S_2 of an aggregate S_3; depending on the grayscale depth, N is the number of levels of I within its range of validity (e.g., 256 for a 8-bit grayscale depth). The subset $S_2(I \geq I^*) = S_{2,I^*}$ is defined as the set of pixels with $I \geq I^*$; because every subset S_{2,I^*} has a perimeter-based fractal dimension $d_P(S_{2,I^*}) = d_{P,I^*}$, then the set S_2 is associated with N subsets $S_{2,I}$ and N perimeter-based fractal dimensions $d_{P,I}$. The set of points defined by I and $d_{P,I}$ is the perimeter-based fractal dimension spectrum. Note that d_{P,I^*} is defined as in Eq. (4) with $N_P = N_P(S_{2,I})$ and $N_A = N_A(S_{2,I})$ the dimensionless perimeter and area of subset $S_{2,I}$.

2.3 Analytical description of the spectrum

Light intensity I is not uniformly distributed across the projection S_2 when irregular aggregates are characterized by surface asperities. Hence, from a conceptual point of view, every subset $S_{2,I}$ is expected to be distinct from one another and be associated with information regarding surface characteristics of S_2 at that I. Consider projections of granular aggregates as in Fig. 1; the first subset $S_{2,0}$ at the lowest intensity shows the exterior outlook of the

aggregate with some level of segmentation, while $S_{2,0<I<1}$ reveals how interior parts of S_2 become increasingly more heterogeneous and segmented as I increases, thus, unfolding the fractal nature of the aggregate surface. With emerging fractal characteristics, $d_{P,I}$ is generally expected to increase from $d_{P,0}$ of the outermost boundary to reach a maximum at some intermediate intensity. However, as I increases to 1, subsets $S_{2,I\to1}$ would show less heterogeneity and segmentation and would eventually collapse into a projection $S_{2,1}$ with ideally no perimeter segmentation (Fig. 1); in this instance, $d_{P,1} = Z(\ell)$ as per Eq. (5).

Because the surface characteristics of aggregates with low $d_0(S_3)$ are expected to be distinct from those with high $d_0(S_3)$, the spectrum $d_{P,I}$ of an aggregate is presumed to depend on $d_0(S_3)$. For example, consider an aggregate A with high $d_0(S_3)$ and an aggregate B with low $d_0(S_3)$ (Fig. 1); subsets $S_{2,I}$ of A are expected to be less segmented than those of B. This implies that A would show lower values of $d_{P,I}$ at intermediate intensity as compared to B, signifying that the concavity of spectra decreases as $d_0(S_3)$ increases.

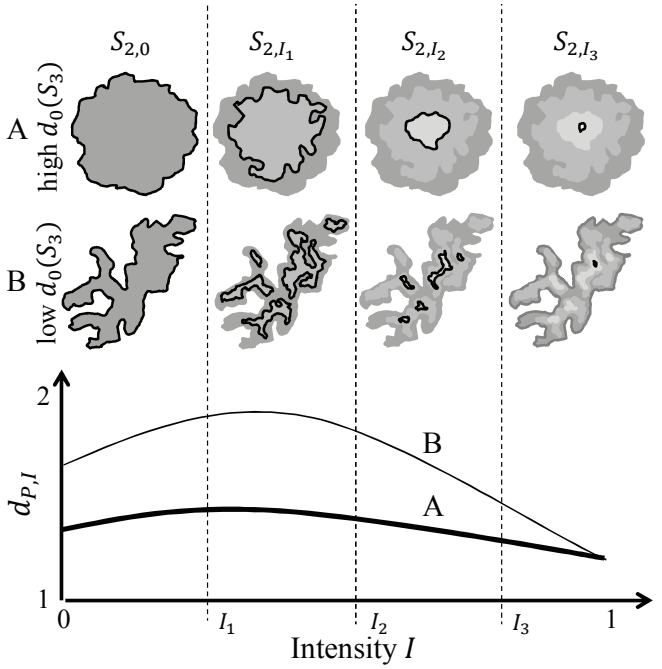

Fig. 1 Conceptual perimeter-based fractal dimension spectra $d_{P,I}$ of S_2 projections of aggregates with high and low capacity dimension $d_0(S_3)$.

Since $d_{P,I}$ may increase from $d_{P,0}$ at $I = 0$ to a maximum value, and eventually decrease to $Z(\ell)$ at $I = 1$, $d_{P,I}$ may be described by a nonlinear (second-order) function of I as

$$d_{P,I} = AI^2 + BI + C. \tag{6}$$

To determine A, B and C in Eq. (6), three conditions are required:

Condition 1 (for $I = 0$): By substituting $I = 0$ into Eq. (6), we obtain

$$C = d_{P,0}, \tag{7}$$

where $d_{P,0}$ is the outermost perimeter-based fractal dimension as in Eq. (4).

Condition 2 (for $I = 1$): Because the spectrum $d_{P,I}$ would eventually be $d_{P,I} = Z(\ell)$ at $I = 1$, using Eq. (6) with $C = d_{P,0}$ as in Eq. (7) allows writing B as a function of A as,

$$B(A) = Z(\ell) - d_{P,0} - A, \tag{8}$$

where $Z(\ell)$ is the known function of Eq. (5).

Condition 3 $\left(\textit{for } \frac{\mathrm{d}d_{P,I}}{\mathrm{d}I} \textit{ and } \frac{\mathrm{d}^2 d_{P,I}}{\mathrm{d}I^2}\right)$: To reflect the characteristics of the spectrum qualitatively depicted in Fig. 1, the first derivative of Eq. (6) has to be positive at $I = 0$ and the second derivative has to be negative as

$$\left.\frac{\mathrm{d}d_{P,I}}{\mathrm{d}I}\right|_{I=0} = B(A) \geq 0, \tag{9a}$$

$$\frac{\mathrm{d}^2 d_{P,I}}{\mathrm{d}I^2} = 2A \leq 0, \forall I. \tag{9b}$$

Assuming that Eqs. (9) are linearly proportional to each other by a factor α, then it is possible to write

$$\frac{\mathrm{d}^2 d_{P,I}}{\mathrm{d}I^2} = -\alpha \left.\frac{\mathrm{d}d_{P,I}}{\mathrm{d}I}\right|_{I=0}, \tag{10}$$

$$2A = -\alpha B(A), \tag{11}$$

$$A = -\frac{\alpha(Z(\ell) - d_{P,0})}{2-\alpha}, \tag{12}$$

where $B(A)$ of Eq. (8) was used in Eq. (11). By making A and $B(A)$ explicit in Eqs. (9), then we obtain

$$\left.\frac{\mathrm{d}d_{P,I}}{\mathrm{d}I}\right|_{I=0} = \frac{2}{2-\alpha}(Z(\ell) - d_{P,0}) \geq 0, \tag{13a}$$

$$\frac{\mathrm{d}^2 d_{P,I}}{\mathrm{d}I^2} = -\frac{2\alpha}{2-\alpha}(Z(\ell) - d_{P,0}) \leq 0. \tag{13b}$$

Because $d_P(S_2) \in [Z(\ell), 2]$, then $(Z(\ell) - d_{P,0}) \leq 0$ and Eqs. (13) satisfy the disequalities only if $(2-\alpha) \leq 0$, that is, only if $\alpha \geq 2$. When $\alpha \to 2$, $\mathrm{d}d_{P,I}/\mathrm{d}I \to \infty$ for $I \to 0$ (Eq. (13a)) and $\mathrm{d}^2 d_{P,I}/\mathrm{d}I^2 \to -\infty$ (Eq. (13b)); on the other hand, $\mathrm{d}d_{P,I}/\mathrm{d}I \to 0$ for $I \to 0$ while $\mathrm{d}^2 d_{P,I}/\mathrm{d}I^2 \to 2(Z(\ell) - d_{P,0})$ when $\alpha \to \infty$. Even though $\alpha \to \infty$ satisfies the conditions in Eqs. (13), a finite value of α has to be assumed to practically use Eq. (10); hence, an arbitrary value $\alpha = \tilde{\alpha}$ is introduced here, while an explicit value is derived later in Sec. 3.

As conceptually depicted in Fig. 1, $\mathrm{d}^2 d_{P,I}/\mathrm{d}I^2$ is not constant but is a function of $d_0(S_3)$ through α. Note also that $d_0(S_3)$ is the unknown that we aim to determine and, therefore, α has to be written as a function of $d_{P,0}$ instead. Because $\mathrm{d}^2 d_{P,I}/\mathrm{d}I^2 \to -\infty$ is expected for aggregates with an infinitely segmented perimeter (*i.e.,* $d_P(S_2) = 2$), then $\alpha = 2$ for $d_{P,0} = 2$; in contrast, $\mathrm{d}^2 d_{P,I}/\mathrm{d}I^2 \to 2(Z(\ell) - d_{P,0})$ is expected for aggregates with no perimeter segmentation (*i.e.,* $d_P(S_2) = Z(\ell)$), hence, $\alpha = \tilde{\alpha}$ for $d_{P,0} = Z(\ell)$. In the absence of substantial evidence of the order of the function $\alpha(d_{P,0})$, the linear function

$$\alpha = \frac{(\tilde{\alpha} - 2)}{Z(\ell) - 2} d_{P,0} + \frac{2(Z(\ell) - \tilde{\alpha})}{Z(\ell) - 2}, \tag{14}$$

was used with $\alpha \in [2, \tilde{\alpha}]$ and with $Z(\ell)$ defined in Eq. (5). The

value of A in Eq. (12) can be calculated by knowing the value of α from Eq. (14).

Finally, using Eqs. (12), (8) and (7) from *Conditions 1, 2* and *3*, the parameters A, B and C that determine the analytical spectrum $d_{P,I}$ in Eq. (6) are

$$A = -\frac{[(\tilde{\alpha}-2)d_{P,0}+2(Z(\ell)-\tilde{\alpha})][Z(\ell)-d_{P,0}]}{(2-d_{P,0})(\tilde{\alpha}-2)}, \tag{15a}$$

$$B = [Z(\ell)-d_{P,0}]\left(1+\frac{(\tilde{\alpha}-2)d_{P,0}+2[Z(\ell)-\tilde{\alpha}]}{(2-d_{P,0})(\tilde{\alpha}-2)}\right), \tag{15b}$$

$$C = d_{P,0}. \tag{15c}$$

where $\tilde{\alpha}$ is a known arbitrary constant, $Z(\ell)$ is calculated from Eq. (5), $d_{P,0}$ is assessed from the outermost boundary of S_2 using Eq. (4), and ℓ can be any positive value. Note that because A, B and C are functions of ℓ, the spectrum $d_{P,I}(\ell)$ is also a function of ℓ.

Global maximum: Since $d_{P,I}(\ell) \in [Z(\ell),2]$, the global maximum $d_{P,\hat{I}}$ of Eq. (6) should not exceed 2. If $d_{P,\hat{I}} > 2$, we impose $d_{P,\hat{I}} = 2$. The parameters A and B are then recalculated in terms of the intensity $\hat{I}$ that yields $d_{P,\hat{I}}$ by equating the first derivative of Eq. (6) to zero. We then obtain

$$A = \frac{d_{P,0}-Z(\ell)}{2\hat{I}-1}, \tag{16a}$$

$$B = Z(\ell) - d_{P,0} - \frac{d_{P,0}-Z(\ell)}{2\hat{I}-1}. \tag{16b}$$

The values of $\hat{I}$ corresponding to $d_{P,\hat{I}} = 2$ can be determined by substituting Eqs. (16) and (7) for A, B and C into Eq. (6), which returns the quadratic function $(Z(\ell)-d_{P,0})\hat{I}^2 + 2(d_{P,0}-2)\hat{I} + 2 - d_{P,0} = 0$. Of the two solutions, only $\hat{I} \in [0,1]$ is valid for this problem.

2.4 The optimal perimeter-based fractal dimension

Among the N subsets $S_{2,I}$, there exists a subset $S_{2,\mathring{I}}$ that yields the optimum $d_{P,\mathring{I}}$ to estimate $d_0(S_3)$ of an aggregate. Note that, $d_{P,\mathring{I}}$ can be any point within the spectrum $d_{P,I}(\ell)$, but $d_{P,\mathring{I}} = d_{P,0}$ is very unlike because $d_{P,0}$ only provides segmentation of the outermost boundary. This may be a possible explanation of why the method in [23] underestimated $d_0(S_3)$ of DLA and CCA aggregates tested in [25]. We then define a continuous function $f(\ell)$ of ℓ that intersects the analytical spectrum $d_{P,I}(\ell)$ and identify $d_{P,\hat{I}}$ as

$$(\mathring{I}(\ell), d_{P,\hat{I}}(\ell)) = d_{P,I}(\ell) \cap f(\ell). \tag{17}$$

The function $f(\ell)$ is not known theoretically but an empirical expression for it will be presented along with experiments in Sec 3. The derivation of $d_{P,\hat{I}}(\ell)$ is considered semi-analytical as it involves both analytical (*i.e.,* $d_{P,I}(\ell)$) and empirical components (*i.e.,* $f(\ell)$). After determining $d_{P,\hat{I}}(\ell)$ from Eq. (17), $d_0(S_3)$ can then be reconstructed using Eq. (2) with $d_P(S_2) = d_{P,\hat{I}}(\ell)$.

2.5 Control set of test aggregates

The semi-empirical method developed above was validated against a control set of different aggregates, including numerically-generated and stereolithographically-fabricated aggregates with known $d_0(S_3)$ and experimentally-acquired aggregates with benchmark values of $d_0(S_3)$.

Numerically-generated aggregates: Particle aggregation governed by different kinetics would normally produce aggregates of different geometrical structures. In order to account for these differences, diffusion-limited (DLA), cluster-cluster (CCA) and self-correlated (SCA) aggregation kinetics were used.

DLA was introduced by [29] to account for aggregation by Brownian (diffusion) motion that forms branch-like aggregates. CCA allows diffusion and aggregation not only of single particles but also clusters of particles, forming bridged and closed-ring aggregates [21,28,30,31]. SCA aggregates, on the other hand, are produced using static accretion, where particles are randomly attached onto existing ones without involving motion explicitly [23]. The probability of an existing particle to receive a new one depends on an exponential distribution function, where an exponent tunes the resulting $d_0(S_3)$ of that aggregate.

In this work, we used 8 3D DLA and 10 3D CCA aggregates of 1000 primary particles already used in [25]. Additionally, 18 3D SCA aggregates were generated as described above. Hence, a total of 36 numerical aggregates with $d_0(S_3)$ ranging between 1.73 and 2.71 were available to our analyses. Among all, 9 of them were used to determine the function $f(\ell)$ in Eq. (17) and the other 27 were used for validation. A summary of the characteristics of the numerical aggregates is given in Table 1.

Projections $S_{2,x}, S_{2,y}$ and $S_{2,z}$ of numerical aggregates along the three principle directions were computed, and were then converted into 8-bit grayscale images. To assign a grayscale to those images, the light intensity observed at a point of the projected plane was calculated as the number of primary particles located at that point but in the direction normal to the projected plane. For this approach, we used the principle of superposition of the effects along with Mie theory [32], assuming therefore that light scatter is proportional to the mass. This approach may not universally apply to any type of aggregates, but it is particularly suited to aggregates of granular (e.g., sediment, dusts, aerosols, etc.) and biological nature (e.g., cells, microbes clusters, etc.), where individual particles are translucent at those scales. Grayscale projections of numerical aggregates reconstructed using the procedure above resulted in outlook similar to images of natural sedimentary aggregates acquired through experiments (see images in the first three columns as compared to those in the fourth column of Fig. 2(a)).

Table 1 Characteristics of DLA, CCA and SCA numerical aggregates.

Aggregate type	DLA	CCA	SCA
Number of aggregates for calibration	3	3	3
Number of aggregates for validation	5	7	15
Actual $d_0(S_3)$	1.82 - 1.86	1.73 - 1.84	1.91 - 2.71
Primary particles	1000	1000	704 - 8374
Dimensionless size	44	55	31

Stereolithographically-fabricated aggregates: Five of the 18 numerical SCA aggregates described above were fabricated by stereolithography (3D printing) using an Objet Eden-250 3D printing

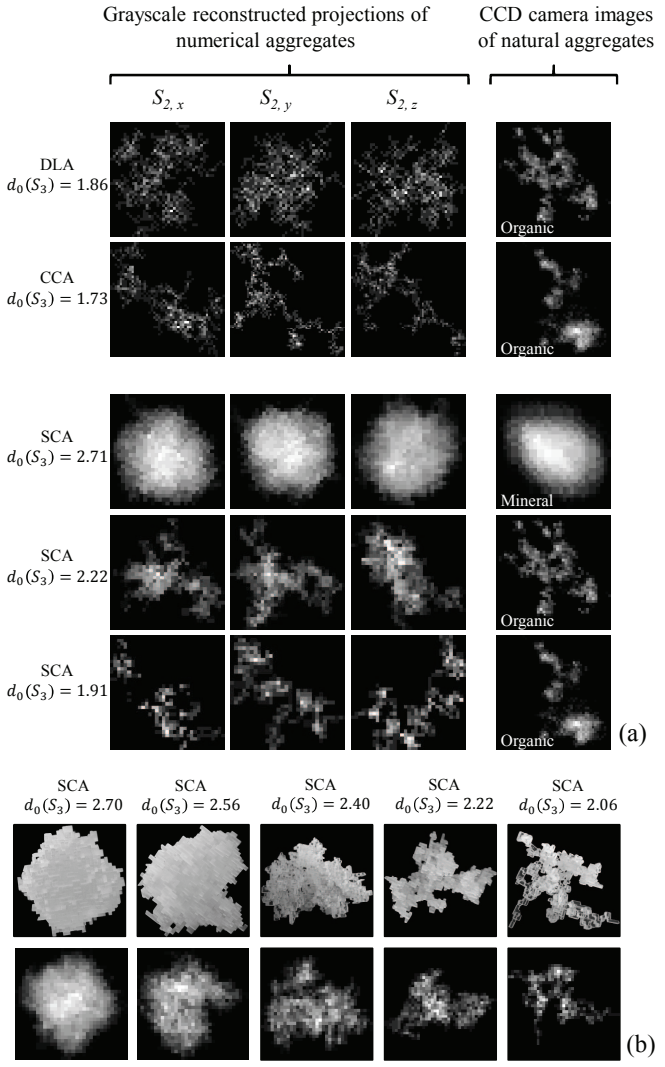

Fig. 2 (a) example grayscale reconstructed projections of diffusion-limited (DLA), cluster-cluster (CCA), and self-correlated (SCA) aggregates in the three principle directions (first three columns) and experimental images of natural sedimentary aggregates (fourth column). (b) example images of stereolithographically-fabricated SCA aggregates (top row) as compared to their grayscale reconstructed projections (bottom row).

apparatus. Aggregates, having 5 cm linear size, were fabricated with Fullcure 720 resin (Objet), which has a specific density of 1.22 g cm^{-3} [33]. For each stereolithographic SCA aggregate, photographic images were acquired in 8-bit grayscale and in three different directions. These images (Fig. 2(b), top row) have relatively similar outlook, though with higher light intensities, as compared to the grayscale reconstructed projections of their corresponding SCA numerical aggregates (Fig. 2(b), bottom row). These images of stereolithographic aggregates were then used for validation.

Experimentally-acquired aggregates: Two types of sediment suspensions were prepared: a natural suspension rich in organic matter collected from Blackwattle Bay, Glebe Council, Sydney, NSW, Australia; and a pure kaolinite suspension (type Q38, with particle size ranging between 0.6 μm to 38 μm). Sampling was conducted using the setup and procedure described in [34]. Aggregate images were acquired in 8-bit grayscale using a μPIV system, which consisted of a CCD camera, a high magnification lens and a white light source. Images were processed with the algorithm described in [34]. Note that both organic and mineral aggregates generally have projections similar to those of numerical aggregates, but they appeared closer to SCA aggregates as compared to DLA and CCA (Fig. 2(a)).

2.6 Statistical estimators

Accuracy of estimations in this study was evaluated using the correlation coefficient $\mathrm{R} = \mathrm{cov}(c,o)/(\sigma_c\sigma_o)$, normalized root mean square error (residuals) $\mathrm{NRMSE} = \left(\frac{1}{n}\sum_{i=1}^{n}(c_i-o_i)^2\right)^{1/2}/(\max\{o\}-\min\{o\})$, and percent error $\mathrm{PE} = |o-c|/o \times 100$, where cov is covariance, c and o are the calculated and observed values, respectively, n is the sample size, and σ_c and σ_o are the standard deviation of c and o, respectively.

3 Results

3.1 Projection-based and analytical spectra $d_{P,I}$ of numerical aggregates

The spectra $d_{P,I}$ of numerical DLA, CCA and SCA aggregates were calculated from their grayscale projections after subsets $S_{2,I}$ were resized to the same ℓ (see dotted lines for three illustrative values of ℓ in Fig. 3(a)-(c)). Projection-based spectra ranged wide intervals in $d_{P,0}$ (at $I=0$), curvature, and $d_{P,1}$ at ($I=1$) regardless of ℓ, but appeared correlated with $d_0(S_3)$ of the original aggregates as conceptually depicted in Fig. 1. In particular, $\mathrm{d}^2 d_{P,I}/\mathrm{d}I^2$ decreased with $d_{P,0}$ decreasing, hence, with $d_0(S_3)$ increasing. All spectra $d_{P,I}$ shared nearly the same value $d_{P,1} < d_{P,0}$ at $I=1$ and had a maximum at intensities $\hat{I} \in [0.25, 0.5]$ for all $d_0(S_3)$ tested here.

This latter feature suggests a way to choose a suitable value $\alpha = \tilde{\alpha}$. By equating the first derivative of Eq. (6) to zero and using Eq. (11), $\hat{I}$ can be expressed as $\hat{I} = -B(A)/2A = 1/\alpha$. If the assumption is taken that $\hat{I} \in [0.25, 0.5]$, then, $\alpha \in [2, \tilde{\alpha}]$ with $\tilde{\alpha} = 4$. Following this line, analytical spectra $d_{P,I}(\ell)$ of all the 36 numerical aggregates were derived based on the procedures described in Sec. 2.3 for $\tilde{\alpha} = 4$ and for $\ell = 2^m$, with $m \in [6, 13]$. Comparison between projection-based and analytical spectra of numerical aggregates are depicted in Fig. 3(a)-(c) only for $\ell = 2^6, 2^8$ and 2^{13}, whereas Fig. 3(d) reports NRMSE and R for all samples and ℓ values. Because $N_P(S_{2,I})$ and $N_A(S_{2,I})$ decreased with I increasing and led to less accurate $d_P(S_2)$, the spectrum for $I \in [0.5, 1]$ was not used in this method. Neglecting these values of the spectrum, we found NRMSE $\leq 20\%$ and R $\geq 90\%$ regardless of ℓ, with slightly better accuracy at high ℓ (Fig. 3(d)).

3.2 Empirical derivation of the function $f(\ell)$

The function $f(\ell) = \hat{I}(d_{P,\hat{I}}(\ell))$ describes the intensity $\hat{I}$ corresponding to the optimum $d_{P,\hat{I}}$ of any spectrum $d_{P,I}(\ell)$ at any ℓ. To empirically derive $f(\ell)$, a calibration set comprising numerical aggregates with known $d_{P,\hat{I}}$ was used, where $d_{P,\hat{I}}$ was calculated from

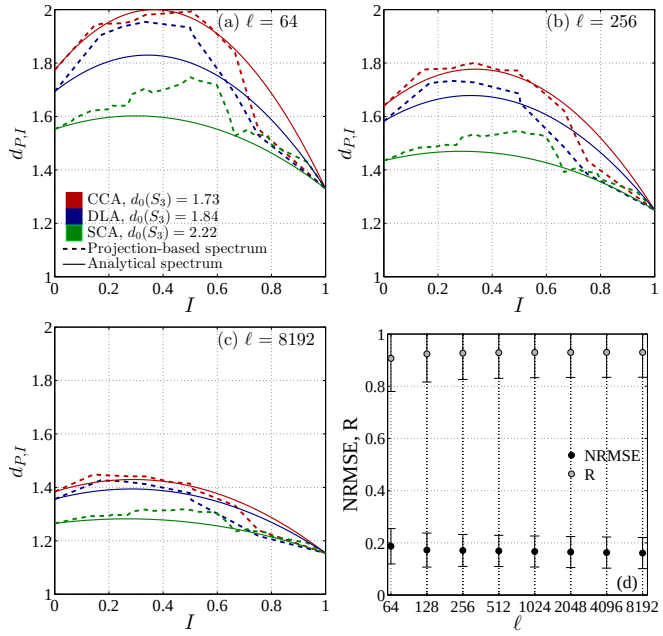

Fig. 3 Example projection-based and analytical spectra $d_{P,I}(\ell)$ of diffusion-limited (DLA), cluster-cluster (CCA), and self-correlated (SCA) numerical aggregates for dimensionless aggregate size: (a) $\ell = 2^6$; (b) $\ell = 2^8$; and (c) $\ell = 2^{13}$. (d) NRMSE and R of analytical spectra $d_{P,I}(\ell)$ against projection-based spectra for all 36 numerical aggregates at different ℓ.

the actual $d_0(S_3)$ by inverting Eq. (2) as

$$d_{P,\mathring{I}}(\ell) = \begin{cases} 2 & \text{for } d_0(S_3) \le k(\ell), \\ \frac{a(\ell)}{[d_0(S_3)]^2} + b(\ell) & \text{for } d_0(S_3) > k(\ell), \end{cases} \tag{18}$$

with $a(\ell)$, $b(\ell)$ and $k(\ell)$ defined in Eq. (3). By knowing $d_{P,\mathring{I}}(\ell)$, the corresponding intensity $\mathring{I}(\ell)$ can be solved for in Eq. (6) by substituting $d_{P,I}(\ell) = d_{P,\mathring{I}}(\ell)$. Solutions lead to three different cases: (i) two solutions $\mathring{I}_1$ and $\mathring{I}_2$ with $\mathring{I} = \max\{\mathring{I}_1, \mathring{I}_2\}$ and $\mathring{I} \in [0,1]$ when $d_{P,\mathring{I}} < d_{P,\hat{I}}$; (ii) one solution of $\mathring{I}$ when $d_{P,\mathring{I}} = d_{P,\hat{I}}$; and (iii) no real solution when $d_{P,\mathring{I}} > d_{P,\hat{I}}$; in this case, $\mathring{I} = \hat{I}$ is imposed. The set of points $(\mathring{I}(\ell), d_{P,\mathring{I}}(\ell))$ relative to the calibration set in Fig. 4(a) shows a trend that can be described by a second order function of the form,

$$f(\ell) = \beta_1(\ell)[d_{P,\mathring{I}}(\ell)]^2 + \beta_2(\ell) d_{P,\mathring{I}}(\ell) + \beta_3(\ell), \tag{19}$$

where $\beta_1(\ell)$, $\beta_2(\ell)$ and $\beta_3(\ell)$ are fitting parameters that depend on ℓ (Fig. 4(b)). We noted that the concavity of $f(\ell)$ increased and that the goodness of fit also increased as a function of ℓ (NRMSE $< 20\%$ and R $> 80\%$, Fig. 4(a) and inset therein). Additionally, fitting parameters showed monotonic trends (increasing or decreasing) as a function of ℓ (Fig. 4(b)). A linear or nonlinear interpolation can be used to obtain specific values of $\beta_1(\ell)$, $\beta_2(\ell)$ and $\beta_3(\ell)$ at any given ℓ.

3.3 Validation against numerically-generated aggregates

A validation set consisting of 27 numerical aggregates (DLA, CCA and SCA) was used to test the accuracy of the method proposed

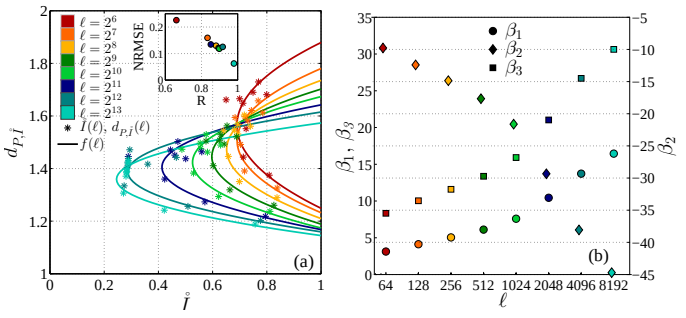

Fig. 4 (a) least square fitting of $f(\ell)$ using calibration coordinates $(\mathring{I}(\ell), d_{P,\mathring{I}}(\ell))$ sets. (b) fitting parameters $\beta_1(\ell)$, $\beta_2(\ell)$, and $\beta_3(\ell)$ of the $f(\ell)$ function in Eq. (19) for dimensionless aggregate size $\ell = 2^m$, with $m \in [6,13]$.

in this study and to compare this method to the earlier approach in[23] for $\ell = 2^m$, with $m \in [6,13]$.

Application of this method persistently achieved a better estimation of $d_0(S_3)$ as compared to the method in[23] regardless of ℓ as shown by statistical quantities in Fig. 5. The method in[23] showed sensitivity to ℓ as PE fluctuated greatly over values of ℓ. In addition, accuracy decreased when the method was applied to aggregates with high $d_0(S_3)$ (Fig. 6); these results agree with those in[27], where greater errors were observed when the method in[23] was used to estimate $d_0(S_3)$ of small lime softening flocs that were expected to have high $d_0(S_3)$.

In contrast, the method proposed in this study showed less sensitivity to ℓ and was able to reconstruct $d_0(S_3)$ at a relatively high accuracy for all $d_0(S_3) \in [1.73, 2.71]$, improving the earlier approach by at least 50% with PE $\le 2\%$ (except for $\ell = 8192$), NRMSE $\le 8\%$ and R $\ge 98.5\%$ (Fig.5). This method also resulted in smaller standard deviation as compared to the method in[23], thus, implying a higher reliability (smaller uncertainty) for all ℓ and $d_0(S_3)$.

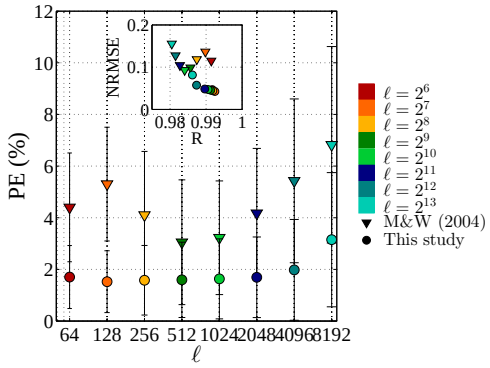

Fig. 5 Percent error PE, normalized root mean square error (residuals) NRMSE and correlation coefficient R of estimated $d_0(S_3)$ for numerical aggregates obtained by using the methods in[23] (M&W (2004)) and in this study.

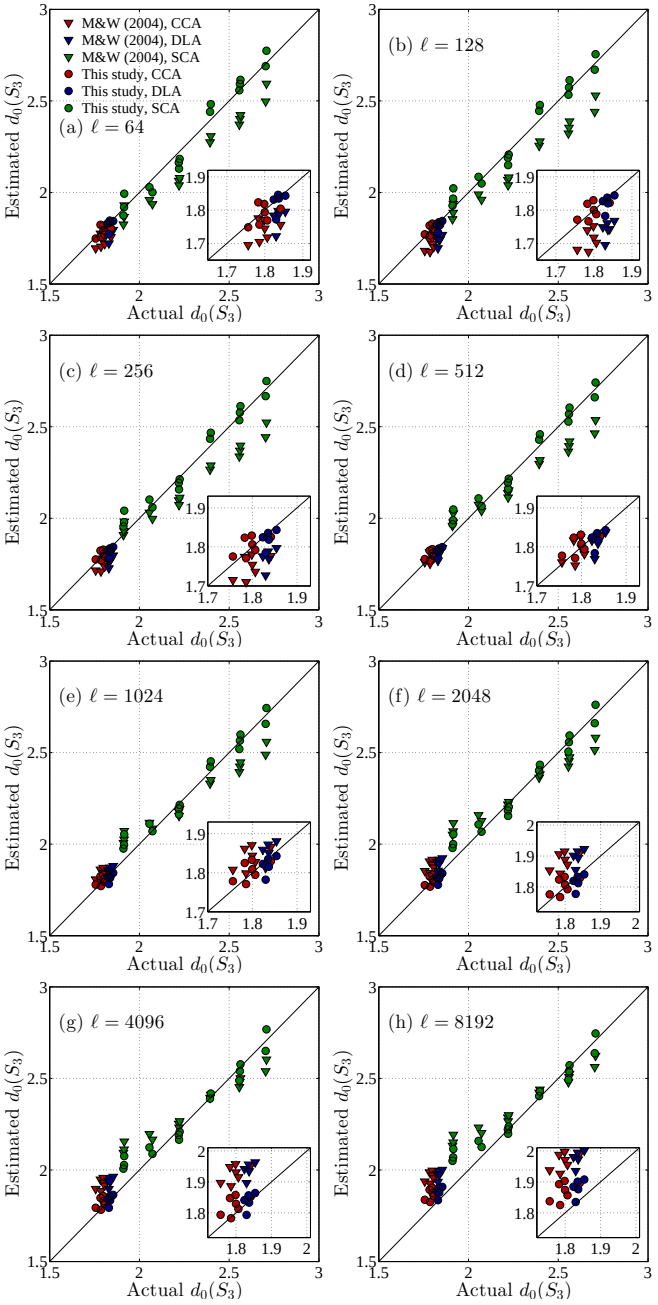

Fig. 6 Estimated $d_0(S_3)$ using the methods in[23] (M&W (2004)) and in this study against actual $d_0(S_3)$ for dimensionless aggregate size $\ell = 2^m$ with $m \in [6, 13]$.

3.4 Validation against stereolithographically-fabricated aggregates

The projection-based spectra $d_{P,I}$ of stereolithographic aggregates showed relatively similar trend to those of numerical aggregates (Fig. 7(a)-(c)), with the spectra increasing from $d_{P,0}$ to eventually converge to $I = 1$ and $d_{P,1} \leq d_{P,0}$. The second half of the spectra, however, showed a steep increase and reached a maximum at $0.9 < \hat{I} < 1$; this was explained by the aggregate showing anisotropicity due to fabrication layering, with material deposited as thin films causing a great light intensity reflected from the surface - images of stereolithographic aggregates in Fig. 2(b) (top row) showed higher light intensities than all other reconstructed and real projections. After excluding $I \in [0.5, 1]$, the analytical spectra $d_{P,I}$ captured the projection-based spectra relatively well for all tested ℓ with NRMSE $\leq 20\%$ (shown in insets of Fig. 7(a)-(c)).

The method in this study achieved $1.8\% < \text{PE} < 3.4\%$ with lower standard deviation in the reconstruction of $d_0(S_3)$ of stereolithographic aggregates as compared to the earlier approach in[23] (PE $> 3.6\%$) for all ℓ tested (Fig. 7(d)).

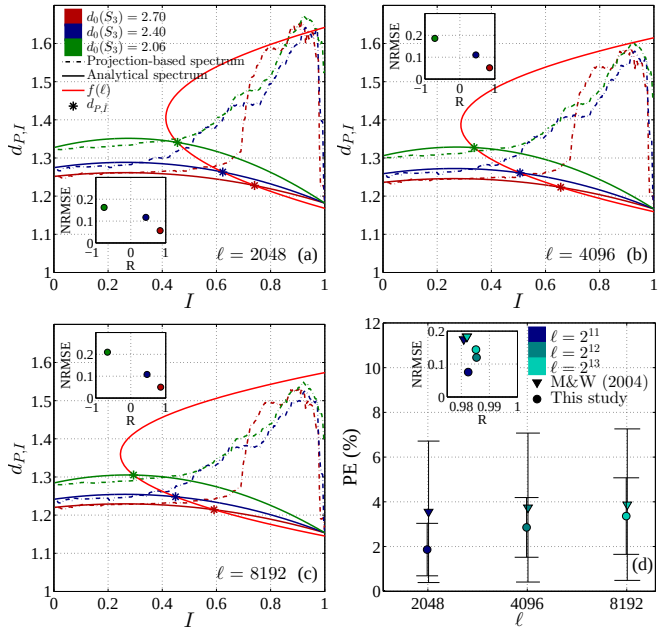

Fig. 7 Projection-based and analytical spectra $d_{P,I}$ of stereolithographic self-correlated (SCA) aggregates for dimensionless aggregate size: (a) $\ell = 2048$; (b) $\ell = 4096$; and (c) $\ell = 8192$. (d) percent error PE, normalized root mean square error (residuals) NRMSE, and correlation coefficient R of estimated $d_0(S_3)$ for stereolithographic aggregates obtained by using the methods in[23] (M&W (2004)) and in this study.

3.5 Application to experimentally-acquired aggregates

For natural aggregates (mineral and organic), $d_0(S_3)$ can be estimated both directly using the method proposed in this study as well as the earlier approach in[23], or indirectly using their settling velocities calculated from images acquired through the experiments described in Sec. 2.5.

When applying the method in this study, we observed that the projection-based spectra $d_{P,I}$ of organic natural aggregates were substantially different from those of mineral aggregates (Fig. 8(a) and(b)). Organic aggregates possessed spectra with distinct curvature and were similar to spectra of numerical aggregates with low $d_0(S_3)$. In contrast, spectra of mineral aggregates were relatively flat. More importantly, the analytical spectra $d_{P,I}$ of both organic and mineral aggregates matched relatively well with the first half of their projection-based spectra (NRMSE $< 16.5\%$ and R $> 95\%$). Application of the method in this study returned $d_0(S_3) \in [2.78, 2.87]$ for mineral aggregates and $d_0(S_3) \in [1.99, 2.15]$ for organic aggregates. On the other hand, the earlier approach in[23] resulted in slightly lower values of $d_0(S_3)$ for both min-

eral ($d_0(S_3) \in [2.56, 2.68]$) and organic ($d_0(S_3) \in [1.94, 2.07]$) aggregates.

To validate estimated $d_0(S_3)$ using 2D optical projections, $d_0(S_3)$ of natural aggregates was also determined from their settling velocities v following the force balance equation $F_g - F_b = F_v + F_i$, where $F_g = \frac{\pi}{6} L^3 \ell^{d_0(S_3)-3} \rho_s g$ is the gravitational force, $F_b = \frac{\pi}{6} L^3 \ell^{d_0(S_3)-3} \rho_f g$ is the buoyancy force, $F_v = 6\sqrt{\pi}\mu v \left(\frac{\pi}{4} L^2\right)^{[(a/d_0(S_3))+b]/2}$ is viscous drag and $F_i = \frac{\pi}{4} L^2 \rho_f v^2$ is impact drag[35]. Here, μ is the fluid dynamic viscosity, g is the gravitational acceleration, L is the characteristic aggregate size, ℓ is the dimensionless aggregate size, ρ_s and ρ_f are the sediment and fluid densities, respectively, whereas $a = 9/8$ and $b = 7/8$ of Eq. (3) were used with experimental data as in[35]. Here, $L_p = 0.6$ μm and $L_p = 2.4$ μm were used for mineral and organic aggregates as per average values in the data base available in[35], while $\mu = 1.0 \times 10^{-3}$ Pa s and $\rho_f = 1000$ kg/m^3 were used.

By knowing the aggregate settling velocity v and the size L from experiments, ρ_s and $d_0(S_3)$ remain unknown in the force balance equation. Fig. 8(c) and (d) show the relationship between ρ_s and $d_0(S_3)$ derived using experimental v and L of both organic and mineral aggregates, respectively. The estimated $d_0(S_3)$ of mineral aggregates yielded 1800 kg/m^3 $< \rho_s <$ 2200 kg/m^3, whereas, the approach in[23] returned $\rho_s \geq$ 2600 kg/m^3. Because kaolinite mineral has a density not generally exceeding 2600 kg/m^3, results using[23] might have lower reliability in this circumstance (note, though, that only a few aggregates were used as an illustration, Fig. 8(d)). In contrast, both methods returned values of ρ_s of organic aggregates that match previous literature[35–37], with the method in this study returning slightly lower values of ρ_s (1700 kg/m^3 $< \rho_s <$ 1800 kg/m^3) as compared to the earlier approach (1800 kg/m^3 $< \rho_s <$ 1900 kg/m^3) (Fig. 8(c)).

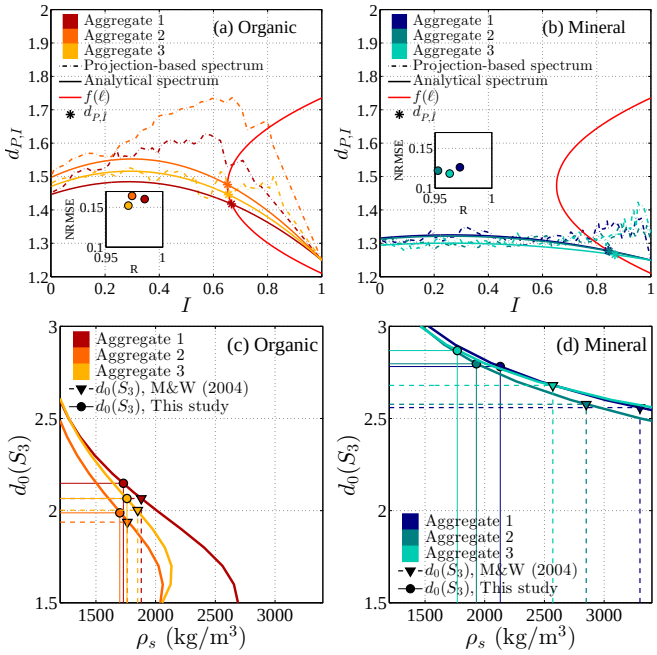

Fig. 8 Projection-based and analytical spectra $d_{P,I}$ of (a) organic and (b) mineral aggregates for dimensionless aggregate size $\ell = 256$; relationship between aggregate density ρ_s and capacity dimension $d_0(S_3)$ according to force balance equation for (c) organic and (d) mineral aggregates.

4 Recommendations

Although the concept that drives the derivation of the method proposed in this study bases on the light intensity spectrum of grayscale images, the application of this method does not require the assessment of the full projection-based spectrum $d_{P,I}$; instead, it requires only the determination of $d_{P,0}$ to derive both the analytical spectrum $d_{P,I}$ and the empirical function $f(\ell)$ used to reconstruct $d_0(S_3)$. This method, therefore, provides a simple and effective alternative to improve estimation of $d_0(S_3)$ of granular aggregates from two-dimensional images. The algorithm of this method (a Matlab function file) is provided as supplementary document.

Even though the applications of this method to different types of aggregates (*e.g.,* DLA, CCA, SCA and natural aggregates) were shown to give good estimation of $d_0(S_3)$ (NRMSE $\leq 10\%$ and R $\geq 98\%$), there exists exceptional cases where the application of this method is biased. For example, derivation of $d_{P,I}$ is not applicable to extensive fractal structures that do not have a definite boundary, case in which this method would not be appropriate. In addition, application of this method to Euclidean solids with fractal surface would result in biased estimation of $d_0(S_3)$; in fact, a fully solid Euclidean body has $d_0(S_3) = 3$ but its planar projection would show significant perimeter segmentation as a result of its surface roughness and, thus, the application of this method to reconstruct its $d_0(S_3)$ would result in false values. Hence, we recommend this method to be particularly suitable for applications with compact fractal sets such as granular aggregates. If part of the projection-based spectrum of a body looks like any of those presented here, it is presumed that the method proposed here can return a reliable estimation of $d_0(S_3)$.

5 Conclusion

A semi-analytical method has been proposed to reconstruct the 3D capacity dimension $d_0(S_3)$ of fractal aggregates from their 2D grayscale projections. The method presented in this study makes use of the light intensity and perimeter segmentation spectrum of an aggregate image to determine the optimum perimeter-based fractal dimension associated to the actual $d_0(S_3)$ of that aggregate. The integration of an analytical expression of the spectrum and an empirical intersecting function derived from fractal granular aggregates of various nature (diffusion-limited, cluster-cluster and self-correlated aggregates) makes the method particularly effective, robust, and user-friendly in that it only requires a binary projection image of the aggregates under investigation. This method resulted in an average error of 2% while an earlier approach resulted in an average error of 4.5%, hence, showing approximately 50% estimation improvement. The algorithm of this method (coded in a Matlab function file) is provided as supplementary document in an open source format.

Acknowledgement

The authors thank three anonymous reviewers for their comments to the original manuscript.

Appendix A: Supplementary documents

The algorithm to estimate $d_0(S_3)$ of a fractal aggregate is provided as an open source Matlab R2011b function file. Together with the function, two grayscale images and two binary images of fractal aggregates are provided as examples.

List of symbols

α,β	[-]	coefficients of Eq. (12) and Eq. (19)
ℓ	[-]	dimensionless aggregate size
μ	[$ML^{-1}T^{-1}$]	fluid dynamic viscosity
ρ_f, ρ_s	[ML^{-3}]	fluid and sediment density
σ_c	[-]	standard deviation of calculated values
σ_o	[-]	standard deviation of observed values
a,b	[-]	coefficient of Eq. (2)
c	[-]	calculated values
cov	[-]	covariance
d_0	[-]	capacity dimension
d_P	[-]	perimeter-based fractal dimension
$d_{P,I}$	[-]	perimeter-based fractal dimension spectrum
$d_{P,\hat{I}}$	[-]	global maximum of $d_{P,I}$ spectrum
$d_{P,\mathring{I}}$	[-]	optimum perimeter-based fractal dimension
$d_{P,0}$	[-]	outermost perimeter-based fractal dimension
$f(\ell)$	[-]	empirical expression for $d_{P,\mathring{I}}$
g	[LT^{-2}]	gravitational acceleration
k	[-]	coefficient of Eq. (3)
n	[-]	sample size
o	[-]	observed values
v	[LT^{-1}]	settling velocity
z	[-]	coefficient of Eq. (3)
A,B, C	[-]	parameters in Eq. (6)
F_b	[MLT^{-2}]	buoyancy force
F_g	[MLT^{-2}]	gravitational force
F_i	[MLT^{-2}]	impact drag
F_v	[MLT^{-2}]	viscous drag
I	[-]	normalized light intensity
$\hat{I}$	[-]	I value corresponded to $d_{P,\hat{I}}$
$\mathring{I}$	[-]	I value corresponded to $d_{P,\mathring{I}}$
L	[L]	aggregate size
L_p	[L]	primary particle size
N	[-]	number of levels of I
N_A, N_P	[-]	dimensionless area and perimeter
NRMSE	[-]	normalized root mean square error
PE	[-]	percent error
R	[-]	correlation coefficient
S_2	[-]	two-dimensional projection
S_3	[-]	three-dimensional body
Z	[-]	d_P of a square

References

1 R. Lakes, *Nature*, 1993, **361**, 511–515.
2 K. Giri, N. P. Bhattacharyya and S. Basak, *Biophysical journal*, 2007, **92**, 293–302.
3 W. Wang and Y. Chau, *Soft Matter*, 2009, **5**, 4893–4898.
4 L. Nicoud, M. Lattuada, A. Yates and M. Morbidelli, *Soft matter*, 2015, **11**, 5513–5522.
5 T. S. Khire, J. Kundu, S. C. Kundu and V. K. Yadavalli, *Soft Matter*, 2010, **6**, 2066–2071.
6 A. G. Marangoni, *Trends in Food Science & Technology*, 2002, **13**, 37–47.
7 L. G. Bremer, T. van Vliet and P. Walstra, *Journal of the Chemical Society, Faraday Transactions 1: Physical Chemistry in Condensed Phases*, 1989, **85**, 3359–3372.
8 A. Carpinteri, P. Cornetti, N. M. Pugno and A. Sapora, Advances in Science and Technology, 2009, pp. 54–59.
9 S. Ahn and S. J. Lee, *Soft matter*, 2014, **10**, 3897–3905.
10 J. P. Hyslip and L. E. Vallejo, *Engineering Geology*, 1997, **48**, 231–244.
11 H. G. E. Hentschel and I. Procaccia, *Physica D: Nonlinear Phenomena*, 1983, **8**, 435–444.
12 H. E. Stanley and P. Meakin, *Nature*, 1988, **335**, 405–409.
13 A. Chhabra and R. V. Jensen, *Physical Review Letters*, 1989, **62**, 1327.
14 A. Khelifa and P. S. Hill, *Journal of Hydraulic Research*, 2006, **44**, 390–401.
15 F. Maggi, *Journal of Geophysical Research: Oceans (1978–2012)*, 2007, **112**, year.
16 U. Skoglund and B. Daneholt, *Trends in Biochemical Sciences*, 1986, **11**, 499–503.
17 P. A. Midgley and M. Weyland, *Ultramicroscopy*, 2003, **96**, 413–431.
18 W. A. Kalender, *Physics in medicine and biology*, 2006, **51**, R29.
19 H. E. Cline, C. L. Dumoulin, H. R. Hart Jr, W. E. Lorensen and S. Ludke, *Magnetic Resonance Imaging*, 1987, **5**, 345–352.
20 L. P. Clarke, R. P. Velthuizen, M. A. Camacho, J. J. Heine, M. Vaidyanathan, L. O. Hall, R. W. Thatcher and M. L. Silbiger, *Magnetic resonance imaging*, 1995, **13**, 343–368.
21 T. Vicsek, *Fractal growth phenomena*, World Scientific, 1989, vol. 4.
22 B. R. Hunt and V. Y. Kaloshin, *Nonlinearity*, 1997, **10**, 1031.
23 F. Maggi and J. C. Winterwerp, *Physical Review E*, 2004, **69**, 011405.
24 N. Sánchez, E. J. Alfaro and E. Pérez, *The Astrophysical Journal*, 2005, **625**, 849.
25 F. Maggi, *Nonlinear Processes in Geophysics*, 2008, **15**, 695–699.
26 P. Domínguez-García and M. A. Rubio, *Colloids and Surfaces A: Physicochemical and Engineering Aspects*, 2010, **358**, 21–27.
27 A. Vahedi and B. Gorczyca, *Water research*, 2011, **45**, 545–556.
28 P. Meakin, *Fractals, scaling and growth far from equilibrium*, Cambridge university press, 1998, vol. 5.
29 T. A. Witten Jr and L. M. Sander, *Physical review letters*, 1981, **47**, 1400.
30 P. Meakin, *Physical Review Letters*, 1983, **51**, 1119.
31 M. Kolb, R. Botet and R. Jullien, *Physical Review Letters*, 1983, **51**, 1123.
32 G. Mie, *Ann. Phys*, 1908, **25**, 377–445.
33 F. Maggi, *Journal of Hydrology*, 2015, **528**, 694–702.
34 F. H. M. Tang, F. Alonso-Marroquin and F. Maggi, *Water re-*

search, 2014, **53**, 180–190.

35 F. Maggi, *Journal of Geophysical Research: Oceans*, 2013, **118**, 2118–2132.

36 K. J. Curran, P. S. Hill, T. G. Milligan, O. A. Mikkelsen, B. A. Law, X. Durrieu de Madron and F. Bourrin, *Continental Shelf Research*, 2007, **27**, 1408–1421.

37 D. J. Lee, G. W. Chen, Y. C. Liao and C. C. Hsieh, *Water Research*, 1996, **30**, 541–550.

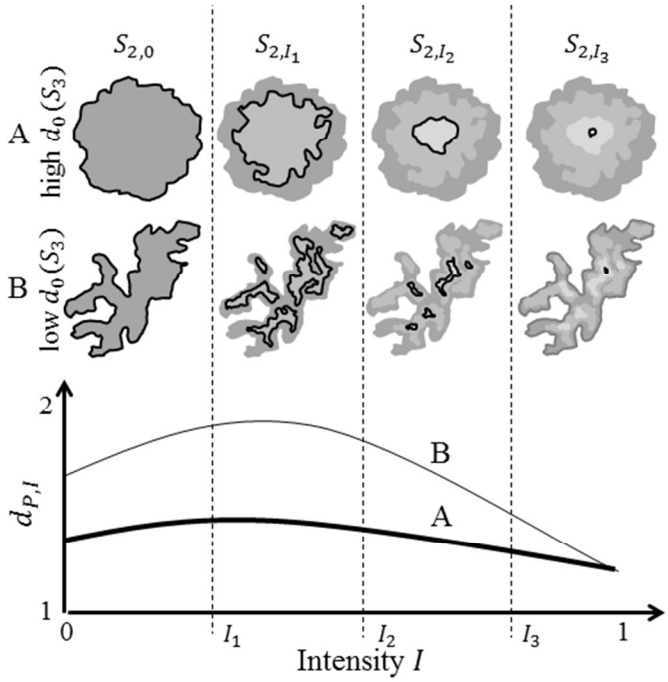

3D capacity dimension $d_0(S_3)$ of aggregates is retrieved using 2D perimeter-based fractal dimension spectrum $d_{P,I}$ that varies with image light intensity.